# Supporting Information

## Novel core-shell structured Fe@$Al_2O_3$ nanofibers by atomic layer deposition as a high-performance microwave absorbent

Xiaoqiang Li [a,*], Jun Xiang [b], Jinnan Yang [b], Kaiyin Zhang [c],

[a] *College of Physics and Electronic Engineering, Xinyang Normal University, Xinyang, 464300, China*

[b] *School of Science, Jiangsu University of Science and Technology, Zhenjiang 212100, China*

[c] *College of mechanical and electrical engineering, Wuyi University, Wuyishan 354300, China*

* *Corresponding author.*

*E-mail address: lxqxynu@163.com (X.Q. Li).*

**Preparation of Fe-NFs**

First, 1.6 g of polyvinylpyrrolidone (PVP, Mw = 1,300,000) was dissolved in a mixed solvent containing 15.2 g of N, N-dimethylformamide (DMF) and ethanol (1:1 by volume). Subsequently, 2.4 g of iron nitrate was added to the above solution, followed by continuous stirring at room temperature for 6 h. Subsequently, electrospinning was carried out on the TL-01 electrospinning equipment at a solution feed rate of 0.5 mL/h and a voltage of 18 kV. The distance from the needle tip to the collector is 18 cm. During the spinning process, the humidity should be controlled between 15% and 30%. The collected electrospinning precursors were vacuum-dried at 80 °C for 12 hours, and then calcined at 500 °C at a heating rate of 2 °C/min for 2 h. The $Fe_2O_3$ nanofibers obtained by calcination were reduced for 1 h in an $H_2$ atmosphere at 400 °C to obtain Fe-NFs.

**Preparation of Fe-NFs@$Al_2O_3$**

0.15g $Fe_2O_3$ sample was ultrasonically dispersed in 10 mL of ethanol solution and then dropped onto the quartz wafer. After drying, the quartz wafer is transferred to the ALD chamber. At a temperature of 300 ℃, with high-purity nitrogen as the carrier gas, trimethylaluminum (TMA) and the precursor $H_2O$ were alternately

introduced into the chamber in the form of pulses, and the number of circulation cycles was set at 300 cycles. After the ALD process was completed, the collected samples were transferred to a tube furnace and reduced for 1 h at 450 °C under $H_2$ atmosphere to obtain Fe-NFs@$Al_2O_3$. For comparison, with all other conditions kept identical, the samples prepared by 200 and 400 cycles of atomic layer deposition are designated as Fe-NFs@$Al_2O_3$-200 and Fe-NFs@$Al_2O_3$-400, respectively.

**Characterizations**

The crystal structure and phase composition of the composites were identified using X-ray diffraction (XRD, D8 Advance) with Cu Kα (λ=0.15418 nm) radiation in the 2θ angle range of 20°–70°. The surface morphology and elemental composition were characterized by field-emission scanning electron microscope (SEM, JEOL JSM-6480). The microstructure was observed via high-resolution transmission electron microscopy (TEM, JEOL JEM-2001 F) operated at 200 kV. Surface chemical compositions and valence states were determined through X-ray photoelectron spectroscopy (XPS). The spectra were collected on a ESCALAB 250Xi system equipped with a monochromatic Al Kα X-ray source. The room-temperature magnetic properties were investigated using a vibrating sample magnetometer (VSM, HH-20) under an applied field of 1.5 T.

**EM characteristics**

The relative complex permeability ($\varepsilon_r = \varepsilon' - j\varepsilon''$) and permeability ($\mu_r = \mu' - j\mu''$) of the composites were measured using the coaxial transmission/reflection method on an Agilent N5224A vector network analyzer in the frequency range of 2–18 GHz. The composites used for EM measurement were prepared by uniformly blending the as-prepared sample with paraffin wax (as the binder) in a mass ratio of 3:7 and then pressed into toroidal-shaped specimens with an outer diameter of 7.00 mm and an inner diameter of 3.04 mm.

Based on the Debye theoretical model, the dipolar relaxation process can be described as [1,2]:

$$\varepsilon_r = \varepsilon_\infty + \frac{\varepsilon_s - \varepsilon_\infty}{1 + j2\pi f\tau} = \varepsilon' - j\varepsilon'' \quad (1)$$

in which $\tau$, $\varepsilon_s$, $f$, and $\varepsilon_\infty$ represent the polarization relaxation time, static permittivity, frequency and relative permittivity in infinite frequency region, separately. Thus, $\varepsilon'$ and $\varepsilon''$ can be written as:

$$\varepsilon' = \varepsilon_\infty + \frac{\varepsilon_s - \varepsilon_\infty}{1 + (2\pi f)^2 \tau^2} \tag{2}$$

$$\varepsilon'' = \frac{2\pi f \tau (\varepsilon_s - \varepsilon_\infty)}{1 + (2\pi f)^2 \tau^2} \tag{3}$$

Based on the formula (4) and (5), the relationship between $\varepsilon'$ and $\varepsilon''$ can be further deduced as:

$$\left(\varepsilon' - \frac{\varepsilon_s + \varepsilon_\infty}{2}\right)^2 + \left(\varepsilon''\right)^2 = \left(\frac{\varepsilon_s - \varepsilon_\infty}{2}\right)^2 \tag{4}$$

Each semicircle in the plot of $\varepsilon'$ versus $\varepsilon''$, commonly known as the Cole-Cole or Debye semicircle, corresponds to a Debye dipolar relaxation.

Attenuation constants ($\alpha$) can be expressed by [3]:

$$\alpha = \frac{\sqrt{2}\pi f}{c} \times \sqrt{\left(\mu''\varepsilon'' - \mu'\varepsilon'\right) + \sqrt{\left(\mu''\varepsilon'' - \mu'\varepsilon'\right)^2 + \left(\varepsilon'\mu'' + \varepsilon''\mu'\right)^2}} \tag{5}$$

On the basis of the experimentally determined $\boldsymbol{\varepsilon_r}$ and the $\mu_r$, the RL values of the samples can be assessed from the transmission line theory as the following formulas [4,5]:

$$Z_{in} = Z_0 \sqrt{\mu_r / \varepsilon_r} \tanh[j(2\pi fd / c)\sqrt{\mu_r \varepsilon_r}] \tag{6}$$

$$\mathrm{RL} = 20 \log |(Z_{in} - Z_0) / (Z_{in} + Z_0)| \tag{7}$$

in which $Z_{in}$ symbolizes the input impedance of the absorbent, $Z_0$ stands for the impedance of air, $f$ represents the frequency of the incident EM wave, $d$ and $c$ are the layer thickness and the velocity of light, respectively.

The corresponding frequency diminishes as the absorber thickness grows, complying with the phenomenon of interference cancellation, commonly referred to as the quarter-wavelength ($\lambda$/4) principle, as illustrated in Equation [6]:

$$d = n\lambda / 4 = nc / (4 f_m \sqrt{|\mu_r||\varepsilon_r|}) \quad (n = 1, 3, 5...) \tag{8}$$

where *d* and *f* are the matching thickness and the corresponding frequency, respectively. If *d* and *f* satisfy equation (8), the phase difference between the incident wave and the reflected wave is 180°, and interference cancellation would occur.

**Figures:**

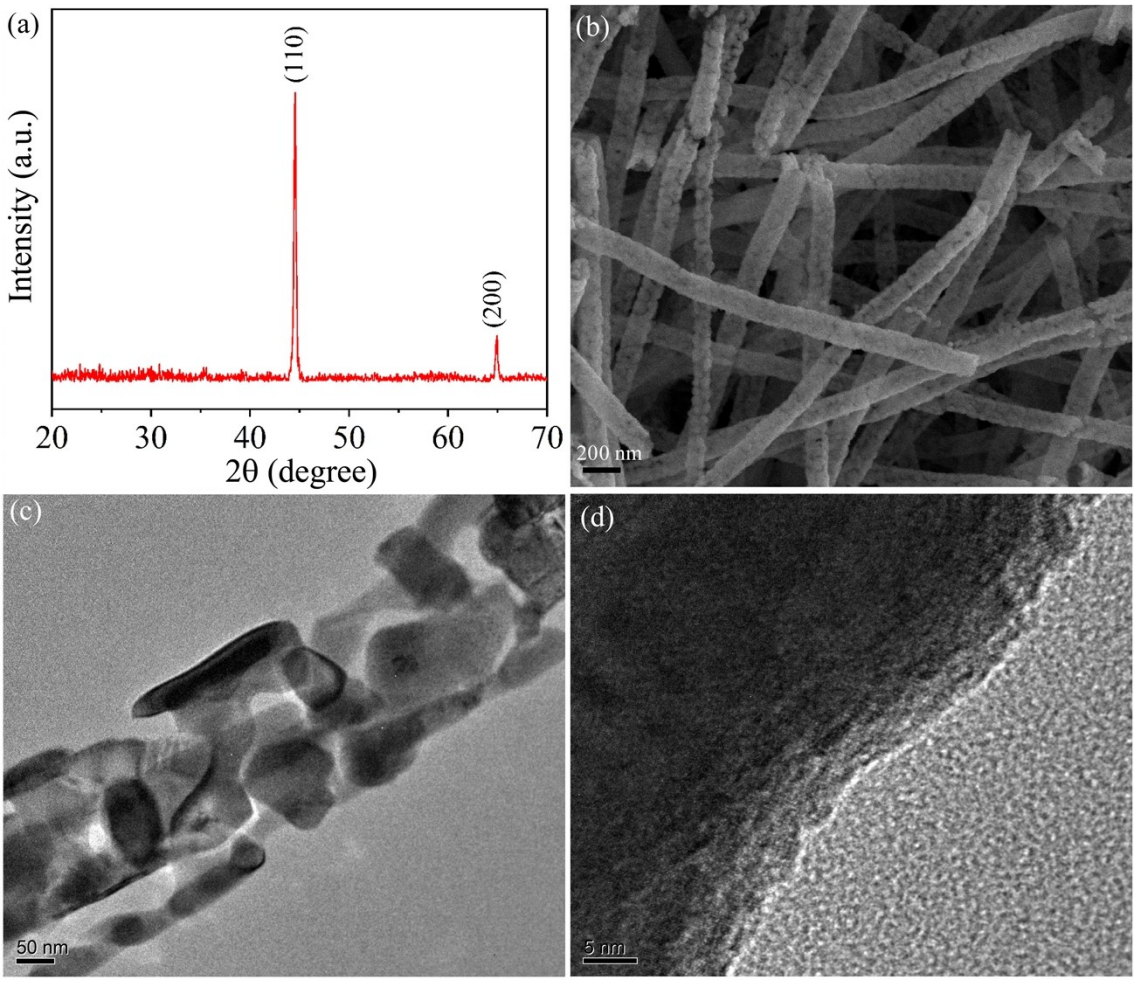


**Fig. S1.** (a) XRD pattern, (b) SEM image, (c) TEM and (d) HRTEM images of Fe-NFs.

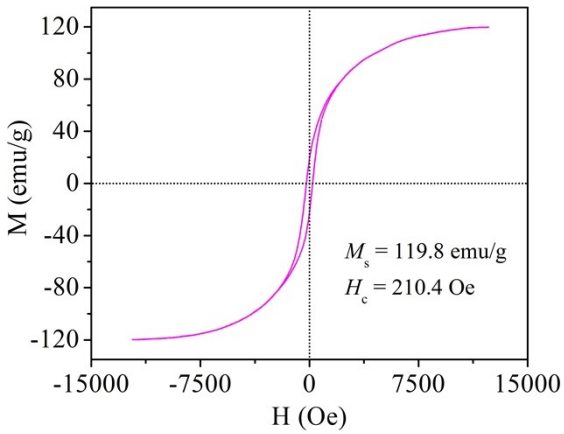


**Fig. S2.** Magnetic hysteresis loop of Fe-NFs.

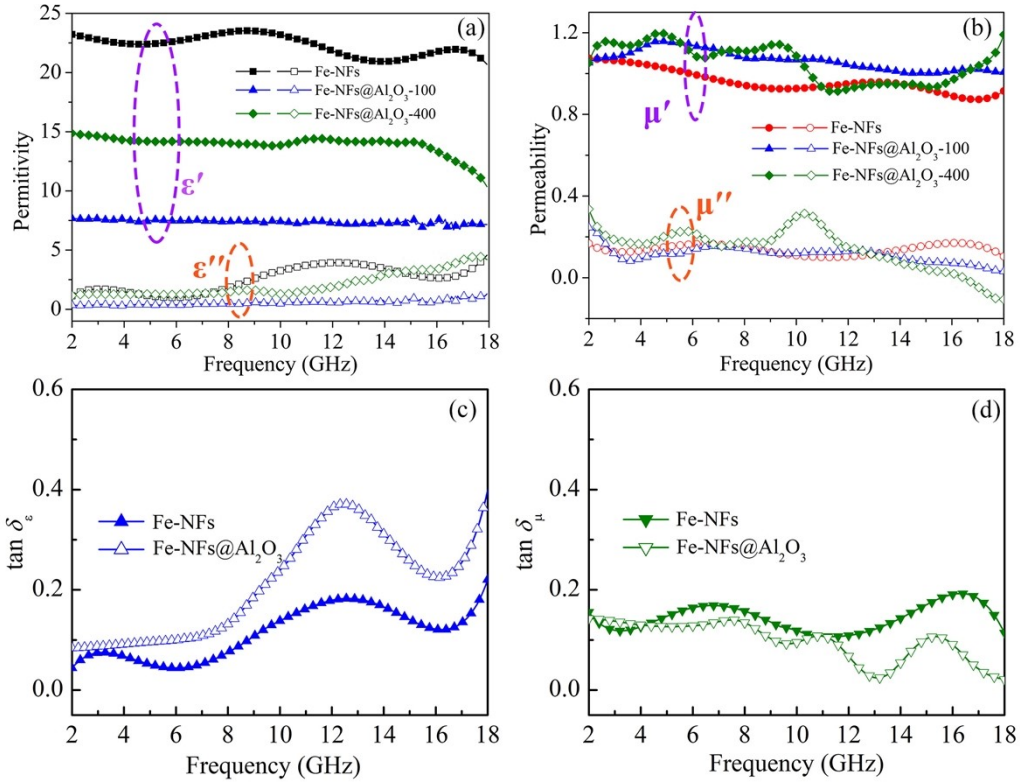


**Fig. S3.** Frequency dependence of (a) complex permittivity and (b) permeability of Fe-NFs, Fe-NFs@$Al_2O_3$-200 and Fe-NFs@$Al_2O_3$-400. Comparison of (c) dielectric loss and (d) magnetic loss between Fe-NFs and Fe-NFs@$Al_2O_3$ in the frequency range of 2–18 GHz.

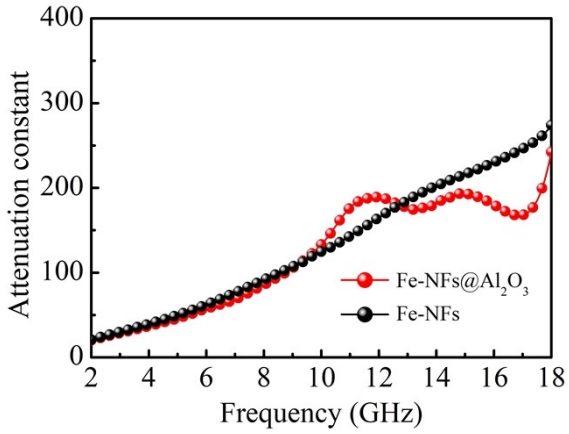


**Fig. S4.** Attenuation constant of Fe-NFs and Fe-NFs@$Al_2O_3$.

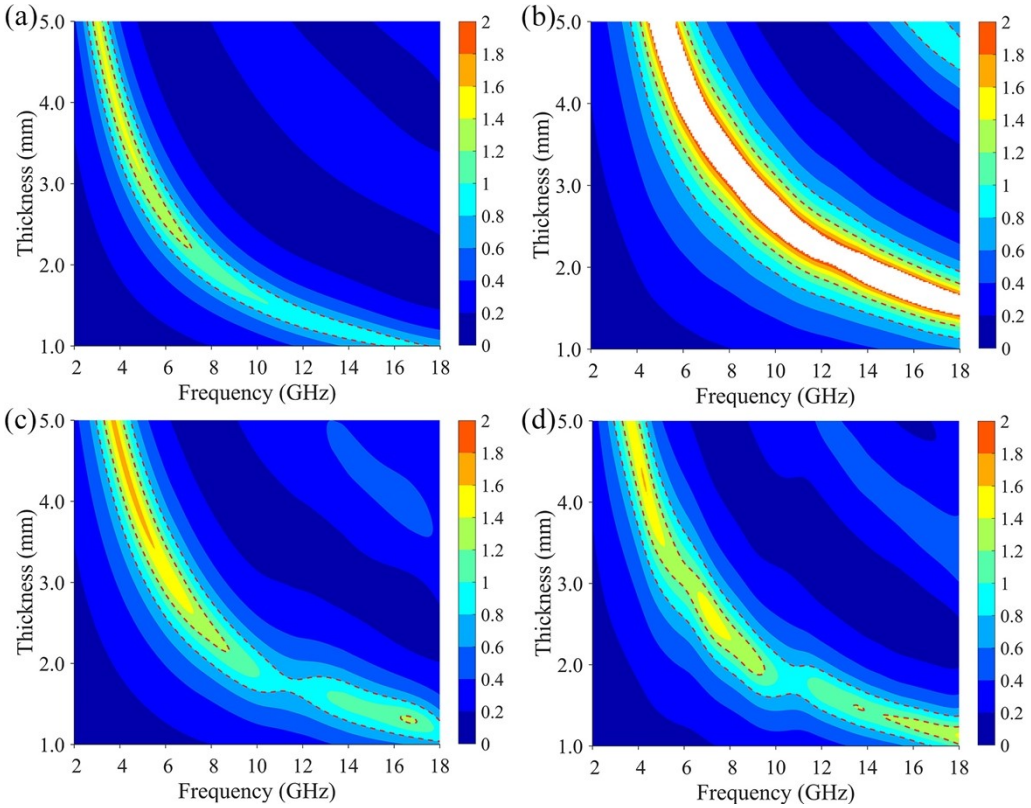


**Fig. S5.** The modulus of normalized input impedance value maps of (a) Fe-NFs, (b) Fe-NFs@$Al_2O_3$-200, (c) Fe-NFs@$Al_2O_3$ and (d) Fe-NFs@$Al_2O_3$-400 at different thicknesses.

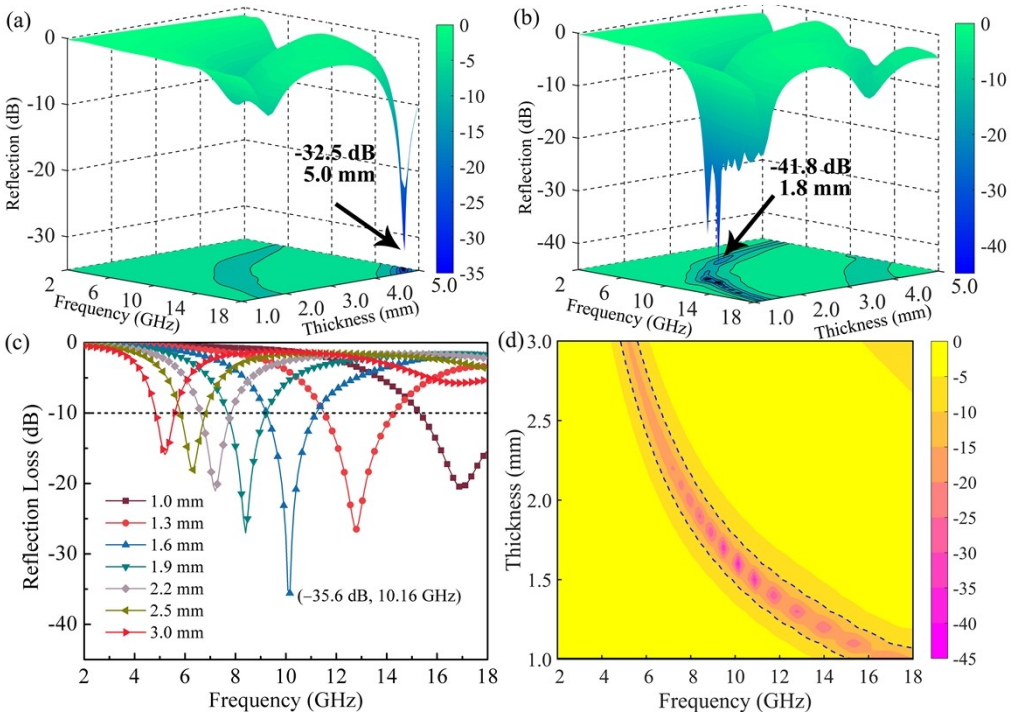


**Fig. S6.** Frequency dependence of RL values for (a) Fe-NFs@$Al_2O_3$-200 and (b) Fe-NFs@$Al_2O_3$-400 at different thicknesses. (c) RL curves and (d) two-dimensional RL map of Fe-NFs with varying absorber thickness in the frequency range of 2–18 GHz (The region confined in the blue dashed lines corresponds to RL < –10 dB).

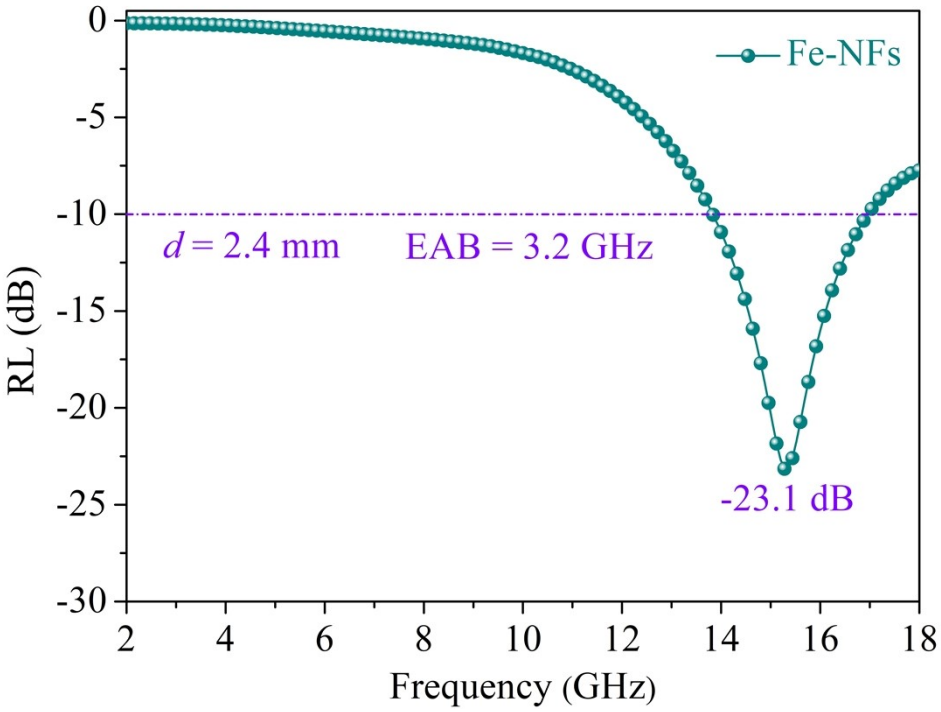


**Fig. S7.** The 2D of RL values and EAB for Fe-NFs

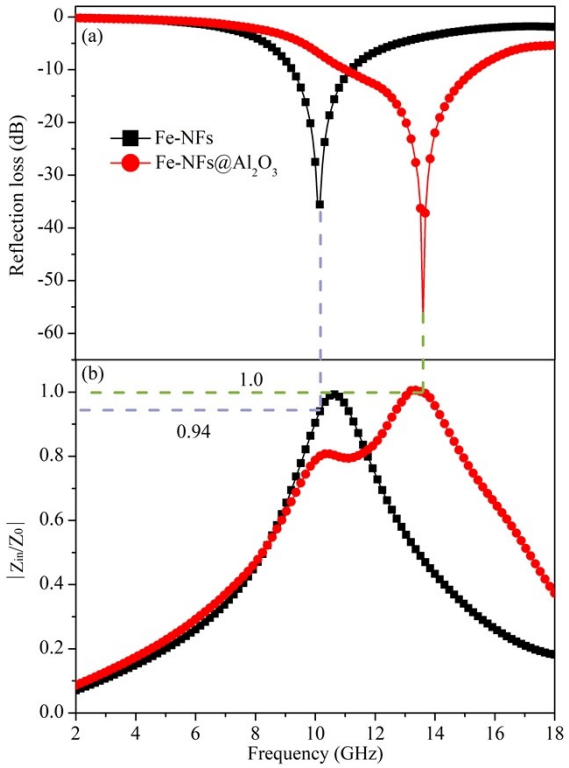


**Fig. S8.** Frequency dependence of (a) RL values and (b) the modulus of normalized input impedance for Fe-NFs and Fe-NFs@$Al_2O_3$.

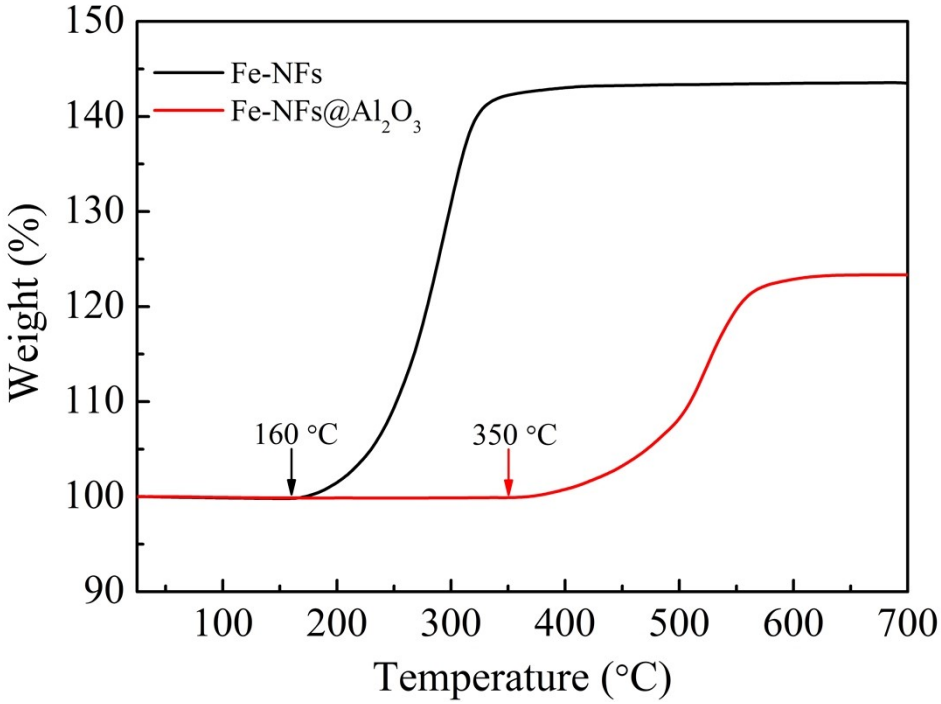


**Fig. S9.** TG curves of Fe-NFs and Fe-NFs@$Al_2O_3$.

**References**

[1] L.L. Xing, H.R. Cheng, Y. Li, Q. Chen, X.H. Liu, Simultaneous manipulation of constituent and structure toward MOFs-derived hollow $Co_3O_4$/Co/NC@MXene microspheres via pyrolysis strategy for high-performance microwave absorption, Chem. Eng. J. 487 (2024) 150729.

[2] J.J. Wang, S.L. Sheng, S.J. Hao, G.T. Liu, R.S. Cai, X.Y. Xue, Y.Q. Wang, Construction of $Fe_{0.64}Ni_{0.36}$@graphite nanoparticles via corrosion-like transformation from $NiFe_2O_4$ and surface graphitization in flexible carbon nanofibers to achieve strong wideband microwave absorption, J. Colloid Interface Sci. 657 (2024) 193–207.

[3] S.J. Wu, H.L. Hou, X. Xue, Quad-band microwave absorbers based on $MoO_{3-x}$@MWCNT with tunable morphologies for multifunctional multiband absorption, Carbon 201 (2023) 1160–1173.

[4] M.R. Tariq, J.F. Wu, M. Ahmad, I. Khan, Z.A. Raza, B.L. Zhang, Preparation and performance of porous

carbon microwave absorber with high porosity from carbonized natural plant fibers, J. Alloys Compd. 1010 (2025) 177490.

[5] C. Wang, J.W. Li, Q.Q. Wang, J.Z. Cao, J.J. Li, L.Y. Chen, H.B. Lu, X.D. He, Structural evolution, microwave absorption performance and in-situ compositing of carbon nanotube prepared from biomass-based citric acid and urea, Surf. Interfaces 55 (2024) 105408.

[6] Z.M. Deng, Y. Li, H.B. Zhang, Y. Zhang, J.Q. Luo, L.X. Liu, Z.Z. Yu, Lightweight Fe@C hollow microspheres with tunable cavity for broadband microwave absorption, Composites, Part B 177 (2019) 107346.